

Tracing Fe K X-ray reverberation lag in the energy-resolved spectra of Narrow-line Seyfert 1 galaxy Ton S180

DILIP KUMAR ROY,¹ SAMUZAL BARUA,^{2,*} RANJEEV MISRA,³ RATHIN SARMA,¹ AND V. JITHESH⁴

¹*Department of Physics, Rabindranath Tagore University, Hojai, 782435, Assam, India*

²*Shanghai Astronomical Observatory, Chinese Academy of Sciences, 80 Nandan Road, Shanghai 200030, China*

³*Inter-University Centre for Astronomy and Astrophysics (IUCAA), PB No. 4, Ganeshkhind, Pune, 411007, India*

⁴*Department of Physics and Electronics, Christ University, Hosur Main Road, Bengaluru 560029, India*

ABSTRACT

We report the Fe K relativistic reverberation feature for the first time in the Narrow-line Seyfert 1 galaxy Ton S180. Using a long observation from *XMM-Newton* we find that the Fe K emission lag peaks at 117 ± 49 s in the lag energy spectrum computed for frequencies $(0.3 - 8.5) \times 10^{-4}$ Hz. The lag amplitude drops to 22.85 ± 14.20 s as the frequency increases to $(8.5 - 30) \times 10^{-4}$ Hz. The time-averaged spectrum of the source shows a relatively narrow Fe K line at ~ 6.4 keV, resulting in black hole spin to be low ($a = 0.43^{+0.10}_{-0.14}$) found from the reflection modelling. We perform general relativistic transfer function modelling of the lag energy spectra individually. This provides an independent timing-based measure of the spin at $a = 0.30^{+0.34}_{-0.17}$, and black hole mass $M_{\text{BH}} = 0.29^{+0.01}_{-0.16} \times 10^8 M_{\odot}$, comparable to the previous measurement, and height of the corona $h = 2.59^{+5.17}_{-0.33} r_{\text{g}}$. Further, we observe that the Fe K lag and the black hole mass fit well in the linear lag-mass relation shown by other Seyfert 1 galaxies.

Keywords: Accretion (14) — Black hole physics (159) — X-ray active galactic nuclei (203) — Reverberation mapping (2019) — Seyfert galaxies (1447)

1. INTRODUCTION

Accretion of matter onto the supermassive black hole plays a key role in the formation and evolution of galaxies. It is known that most X-ray emissions emerge close to the black hole, where the accretion flow becomes progressively active, and major physical phenomena occur. This central region is generally too small to be spatially resolved by the current detectors, except in a few unusual cases. X-ray reverberation approach therefore emerged as a powerful technique that overcomes this limit by using echoes of light, providing insight into the structure and kinematics of matter flowing onto the black hole as well as the X-ray emitting corona (see P. Uttley et al. 2014; E. M. Cackett et al. 2021, for a review).

The interplay of the accretion disc and the corona is known to lead to X-ray emission in AGN. In the standard paradigm, the hard X-ray emission in AGN is a result of Compton up-scattering of the soft photons from the geometrically thin and optically thick accretion disc (N. I. Shakura & R. A. Sunyaev 1973) by the hot elec-

trons in the corona (F. Haardt & L. Maraschi 1991). These X-rays are generally referred to as primary continuum described by the powerlaw, a fraction of which focuses on the accretion disc and is reprocessed, producing the reflection spectrum. The pronounced reflection features often appearing in the X-ray spectrum are the fluorescent Fe K emission line at ~ 6.4 keV and the Compton-hump above ~ 10 keV (I. M. George & A. C. Fabian 1991). The Fe K line profile becomes relativistically broadened due to the combined effect of the gravitational redshift and the Doppler shift (C. S. Reynolds & M. A. Nowak 2003), providing information on the black hole spin, disc inclination and the geometry of the inner accretion disc. While other form of the reflection feature is seen in the soft X-ray excess (J. Crummy et al. 2006), its origin remains a mystery which in some AGNs has been found to originate from a thermal Comptonization component (A. M. Lohfink et al. 2013).

X-ray observations enable us to move beyond spectral modelling and measure the reverberation time delay between the variations of two emission bands. The reverberation time delay is generally attributed to the light travel time between the directly observed continuum from the corona (powerlaw-dominated X-ray band)

Corresponding author: Samuzal Barua

*

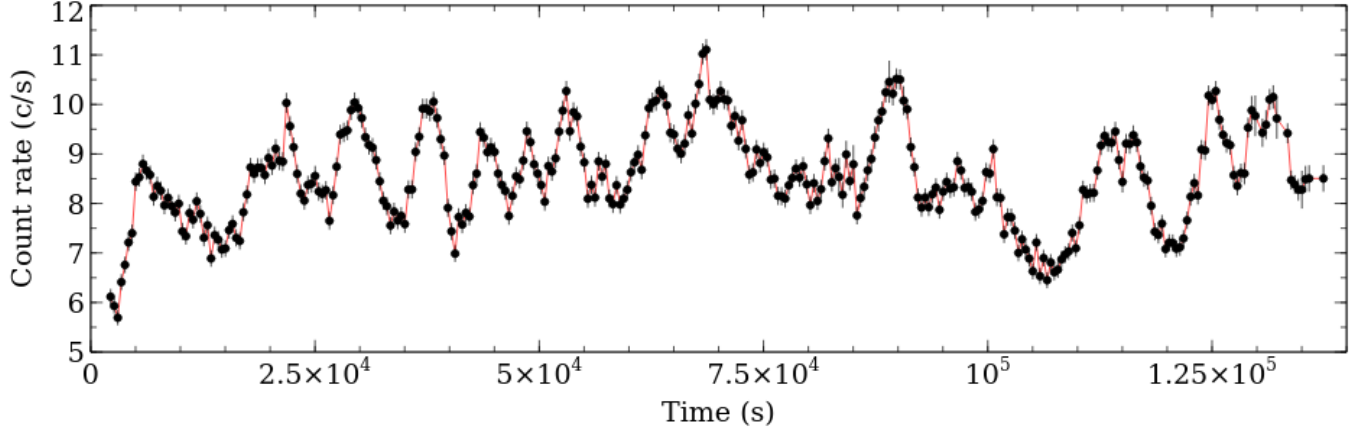


Figure 1. *XMM-Newton* lightcurve of Ton S180 with a 400 s bin size. The lightcurve is extracted from 0.3 to 10 keV.

and the reflected X-rays from the accretion disc (P. Uttley et al. 2014).

Relativistic reverberation feature was detected for the first time in the Narrow-line Seyfert galaxy 1H0707-495 in which soft X-ray in the 0.3–1 keV band was found to lag the 1–4 keV hard continuum by ~ 30 s at high frequencies (A. C. Fabian et al. 2009). Follow-up observations have enabled the detection of soft lag in several other Seyfert galaxies and X-ray binaries (XRBs) (e.g. B. de Marco et al. 2011; A. Zoghbi & A. C. Fabian 2011; S. Tripathi et al. 2011; E. M. Cackett et al. 2013; B. De Marco et al. 2013; E. Kara et al. 2013a; W. N. Alston et al. 2020; E. Kara et al. 2019; J. Wang et al. 2022). The reported soft lags at high frequencies refer to the light travel time between the soft X-ray excess dominated by relativistic reflection and the powerlaw continuum of the corona. Sources also show hard lags in which the powerlaw-dominated hard X-ray band lags the soft band at low frequencies (a.k.a low-frequency hard lag), which has been observed in Galactic black holes and AGNs (e.g. S. Miyamoto & S. Kitamoto 1989; M. A. Nowak et al. 1999; I. M. McHardy et al. 2007; P. Arévalo & P. Uttley 2006; P. Arévalo et al. 2008). The possible origin of the hard lag has been interpreted as a consequence of fluctuation rate variation of the accretion flow that propagates over the disc (P. Arévalo & P. Uttley 2006), also referred to as propagation fluctuation delay. However, the interpretation of the low-frequency lag scenario remains incomplete.

An alternative model was suggested by L. Miller et al. (2010b) to account for the origin of low-frequency hard lag, according to which it is the result of reflection from the far side of the disc, typically from a few $\sim 100R_g$ to $\sim 1000R_g$. Timing analysis was carried out by the authors, reporting the hard lag in the Narrow-line Seyfert 1 galaxy in NGC 4051. The same model was suggested to explain the high-frequency lag measured in 1H0707-

495 (L. Miller et al. 2010a), which, contrasts, however, with the soft-lag interpretation of A. C. Fabian et al. (2009). The follow-up study of A. Zoghbi et al. (2011) on the same source 1H0707-495, further argued that the inner disc reflector is responsible for reverberation origin in the soft X-ray band, as observed in A. C. Fabian et al. (2009).

It has also been revealed that the high-frequency lag is not the only reverberation origin of the soft X-ray band; a clear delayed response in the Fe K emission band appears mostly in supermassive black hole candidates, typically the Seyfert 1 galaxies. This has been interpreted to be a consequence of reverberation from within a few gravitational radii of the black hole. The first Fe K reverberation feature was detected in the bright Narrow-line Seyfert 1 galaxy NGC 4151 by A. Zoghbi et al. (2012), suggesting the delayed response of the red wing of the broad Fe K profile with respect to the continuum variation. Successive campaigns have explored the underlying feature in several sources (e.g. A. Zoghbi et al. 2013; E. Kara et al. 2013a; A. Marinucci et al. 2014; W. N. Alston et al. 2015; E. Kara et al. 2016a).

The Narrow-line Seyfert 1 galaxy Ton S180 is among the objects that shows the Fe K emission feature, making it a plausible candidate for exploring the reverberation lag in the corresponding energy band. A broadband spectral analysis was conducted by D. J. Walton et al. (2013) using a long (100-120 ks) *Suzaku* observation taken in 2006. The authors successfully reproduced the X-ray spectrum by modeling with relativistic reflection. Their analysis suggested a rapidly rotating black hole in Ton S180, with spin constrained at $0.91^{+0.02}_{-0.09}$ – consistent with the scenario in which a black hole grows through prolonged and ordered accretion. The source was found to have little to no intrinsic absorption to complicate the analysis. Reflection spectroscopy was further undertaken by M. L. Parker et al. (2018) using the 2015

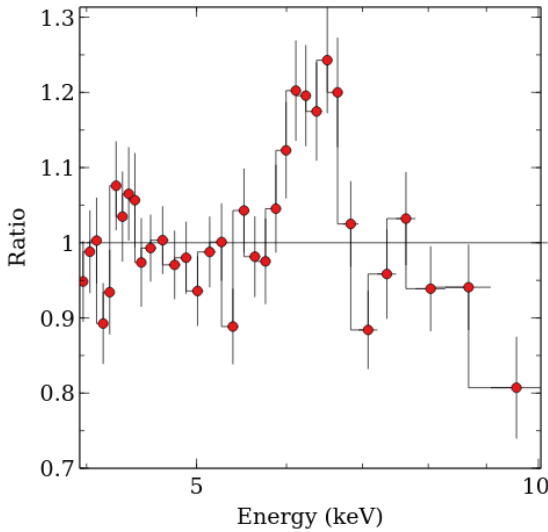


Figure 2. Resolving the Fe K emission line profile, produced from the ratio of the X-ray spectrum to a simple powerlaw model. The data is binned to show only a few points for visual purpose.

XMM-Newton observation. The powerlaw residuals to the spectrum yield a clear Fe K line profile, which appeared to be strong but relatively narrow. The X-ray spectrum of the source cannot be reproduced simply by relativistic reflection – leaving a smoother soft excess. The spectral fit favoured a low spin value of the black hole, which was constrained to be $a < 0.7$. Lastly, [G. A. Matzeu et al. \(2020\)](#) broadly explored the reflection dependency in Ton S180 using 2000-2016 *XMM-Newton* and *NuSTAR* observations, suggesting that the broadband X-ray spectrum can be described by the relativistic reflection combined with (a) disc thermal emission, (b) seed photon comptonisation in an optically thick corona (i.e., warm corona; $kT_e \sim 0.3$ keV), and (c) Comptonisation in the hot ($kT_e \geq 100$ keV) and optically thin corona. Analysis of the spectra with different models provided a black hole spin from low (< 0.34) to high value (> 0.98).

Timing analysis is yet another powerful tool that allows for a model-independent approach to examine the peak Fe K line emission feature by measuring its time delay. In fact, the Fe K emission band is the clearer part of the spectrum, allowing the search for a reverberation signature. In this work, we search for the Fe K reverberation in Ton S180 by computing Fourier lag spectra from one of the long *XMM-Newton* observations. We extend the work to reverberation modelling to constrain the key physical parameters, spin and mass of the black hole, disc inclination as well, and the height of the X-ray corona.

The paper is structured as follows: Section 2 presents the observations and data analysis. The timing analysis is described in Section 3. In Section 4 we report on the modelling of the time-averaged spectrum and lag spectra. The results are discussed and interpreted in Section 5.

2. OBSERVATION AND DATA REDUCTION

2.1. *XMM-Newton*

XMM-Newton conducted the longest observation of Ton S 180 in 2015 July (Obs. ID 0764170101), obtained for a total duration of ~ 141 ks. The lightcurve from this observation is shown in Figure 1, which shows significant X-ray variability with a high count rate; both are particularly useful in the measurement of reverberation lag. We reduced the *XMM-Newton* data with the Science Analysis System (sas v.20.0.0). We used the sas task EVSELECT to create the event file lists for the EPIC-pn detector. The events were cleaned for high background flaring by applying the filtering condition (PATTERN ≤ 4) $\&\&$ (FLAG == 0). We created a Good Time Interval (GTI) to exclude the background flare above an optimal value. The cleaned events were then used to extract the source and background regions. We selected a circular extraction region of 35'' for the source, and a larger background region of 50'' was selected from the source free space. In the following step, we extracted source and background lightcurves using these region files. Finally, background-subtracted lightcurves were produced using the sas task EPICLCCORR.

2.2. *NuSTAR*

NuSTAR observed Ton S180 for an exposure of ~ 127 ks exposure (Obs. ID 60201057002) in 2016. We reduced the data using *NuSTAR* data analysis software NUSTARDAS. The data were screened and processed using the stranded NUPipeline script, which provides Level-1 events. The events were cleaned and calibrated using the most recent version of the calibration database (CALDB; v.20250415). We extracted source counts from a circular region of 50'' in radius, while a larger background region of 90'' was used for both the *NuSTAR* detectors FPMA and FPMB. The source and background spectra were then produced with the NUPRODUCTS task. Finally, we grouped the spectra using the grppha tool so that each spectral bin contains 50 counts.

3. TIME LAG ANALYSIS FOR TON S180

We calculated the lag spectra using the direct Fourier method outlined in [M. A. Nowak et al. \(1999\)](#) and further demonstrated in [P. Uttley et al. \(2014\)](#). We produced 8 different lightcurves of finer energy bins ([2–3,

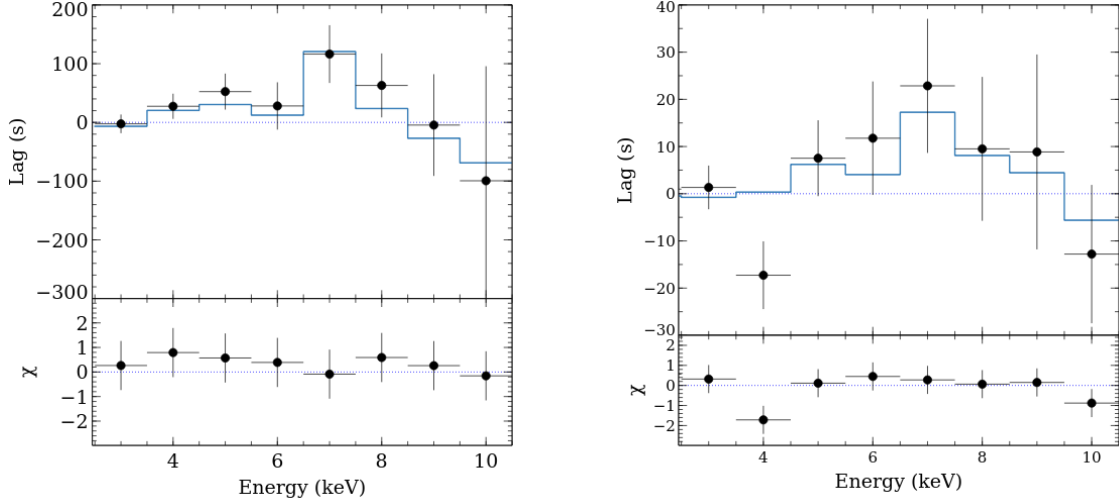


Figure 3. Lags as a function of energy for Ton S180 computed for frequencies $(0.3 - 8.5) \times 10^{-4}$ Hz (left panel) and $(8.5 - 30) \times 10^{-4}$ Hz (right panel). The lag spectra show a clear Fe K emission feature with peak lags of 117 ± 49 s at frequencies $(0.3 - 8.5) \times 10^{-4}$ Hz and 22.85 ± 14.20 s at frequencies $(8.5 - 30) \times 10^{-4}$ Hz. The lags are fitted using the general relativistic transfer function model KYNREVERB. Model lags are represented by the blue steps, whereas the black data points are the computed Fourier lags. Zero lag as a function of energy is shown as the blue dotted line.

3–4, 4–5, 5–6, 6–7, 7–8, 8–9, 9–10] keV) and took their Fourier transformation. The lightcurves were extracted for a bin size of 10 s. We construct the cross-spectrum by multiplying the Fourier transform of the lightcurves by their complex conjugate, which was then averaged over user-defined frequency bins in logarithmic space. The cross-spectrum generally encodes the phase difference between the lightcurves which can eventually be converted into frequency-dependent time lags $\tau(\nu)$ by dividing by $2\pi\nu$, where ν is the center of the defined frequency bins. Fourier lag analysis was carried out using the publicly available code pyLag⁵.

3.1. Lag versus energy

We started by computing the lag energy spectra at different frequency sets. The long observation and small bin size of the lightcurve allow us to calculate lags on a wider frequency range. We used the sign convention, so that positive lags indicate that the band of interest lags the reference band. The reference band here was taken to be the entire 2–10 keV band, except for the bands of interest. A wider reference band was used to increase the signal-to-noise ratio and ensure reduction of the correlated noise between the narrow energy bands.

Computing lags versus energy, we observe that the lag spectra trace the peak lag in the Fe K emission band, 6–7 keV, while the other bands appear to lead relative to this band. The resulting spectra are shown in Figure 3. There appears to be a sharp drop of the lag amplitudes

beyond the 7 keV band, which is typically dominated by the powerlaw emission (directly observed continuum from the corona), while below 4 keV bands are roughly consistent with zero lag. The entire lag spectrum shifts downward with decreasing lags in each energy band as the frequencies increased from $(0.3 - 8.5) \times 10^{-4}$ Hz (left panel) to $(8.5 - 30) \times 10^{-4}$ Hz (right panel), retaining the observed spectrum shape where the Fe K peak lag remains. Frequencies of this order are of particular importance, at which the observed lag spectra replicate the shape of a reflection spectrum, with the Fe K emission feature at ~ 6.4 keV. Interestingly, the shape more mimics the Fe K line profile produced in Figure 2. There appears a dip at 4 keV in the lag energy spectra computed for higher frequencies (Figure 3, right), indicating the earliest response. This feature is more common in the lag energy spectra as a result of relativistic reverberation around the black hole (see also E. Kara et al. 2013b; D. R. Wilkins et al. 2017). We have checked the log-linear trend of the observed lags by using the log-linear model $y = a + b\log(x)$, which provides a poor fit with a χ^2 value of 14 for 8 degrees of freedom for the two frequency ranges. This indicates that we can rule out the null hypothesis of a simple log-linear fit and implies that the energy dependent lag traces the Fe K emission feature.

3.2. Lag versus frequency

Frequency-dependent lags were computed between the two X-ray energy bands: one is the reflection-dominated hard band consisting of Fe K emission peak (taken as the band of interest), and the other is the powerlaw-

⁵ <https://github.com/wilkinsdr/pyLag>

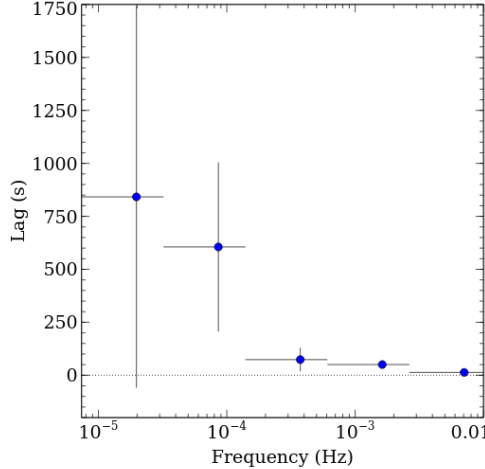


Figure 4. Lag frequency spectrum of Ton S180 computed between the power law-dominated 2–4 keV band and reflection-dominated 4–7 keV band. Positive lags indicate hard lags (4–7 keV hard band lags the 2–4 keV soft band). The lag spectra show a decreasing trend with increasing frequencies, where Fe K emission lag is clear.

dominated soft band (taken as the reference band). Again, we used the same sign convention, in which hard lags are indicated by positive values. The resulting lag spectrum is shown Figure 4. The lag spectrum shows the evolution of lags as a function of the temporal frequency produced between the reflection-dominated 4–7 keV band and the powerlaw-dominated 2–4 keV band. The observed lags follow a trend with the lag decreasing with increasing frequency similar to other Narrow-line Seyfert galaxies (see e.g. MCG-5-23-16 and NGC 7314 (A. Zoghbi et al. 2013)). In the lag spectrum, we see that the Fe K band lag is clear up to a cutoff frequency, above which the lags are observed to decrease promptly, mostly consistent with zero, as the lags are dominated by Poisson noise.

A point to be noted is that since only two narrow energy bands are used in the lag frequency spectrum, the Poisson noise does not allow us to see the lags at further higher frequencies. The energy-dependent lags are, therefore, more reliable for clearly tracing the peak lag in the Fe K band, where the whole energy range (2–10 keV) was taken as a reference.

3.3. Scaling Fe K lag with the black hole mass

The amplitudes of Fe K lags for supermassive black holes have been observed to follow a linear dependence on the black hole mass (see P. Uttley et al. 2014; E. Kara et al. 2016a). Fe K emission lag appears to be larger than the soft excess lags (P. Uttley et al. 2014). Here, we reproduce the plot for Fe K lag versus black hole mass from E. Kara et al. (2016a) (obtained from the

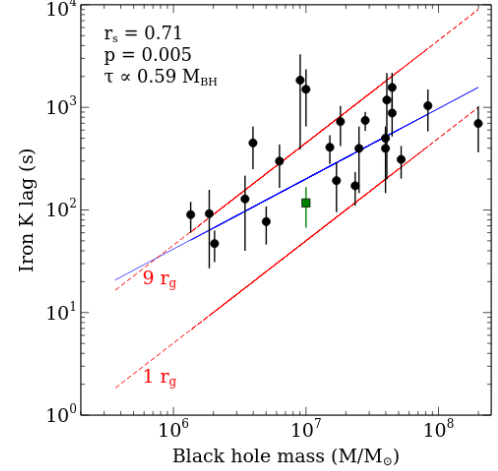


Figure 5. Fe K lag amplitudes versus black hole mass. The plot is reproduced from the published results (shown in black) reported in Table 2 of (E. Kara et al. 2016b), in which our lag measurement in Ton S180 (shown in green) is overplotted. The blue line indicates a linear model used to fit the data, providing a scaling relation of the lag with the black hole mass as $\tau \propto 0.59 M_{\text{BH}}$. The red diagonal lines indicate lag at $1r_g$ and $9r_g$. The Spearman correlation test provides a Spearman rank correlation coefficient of 0.71 at a probability of 0.005.

published results) and include the results for Ton S180 obtained in this work. The resulting plot is shown in Figure 5. We used a linear model to scale the lags as a function of black hole mass, which shows a linear mass dependence of the lags as $\tau \propto 0.59 M_{\text{BH}}$. Furthermore, we estimated the Spearman rank correlation coefficient, $r_s = 0.71$ with a probability $p = 0.005$. These estimates are consistent with the results obtained by E. Kara et al. (2016a) who derived the lag-mass relation for the same sample of type 1 Seyferts. In the plot, the red diagonal lines indicate the lags at $1r_g$ and $9r_g$ for different Seyfert 1 galaxies. When the Fe K lag amplitude measured for Ton S180 is included, it lies within this interval, following the linear trend, further confirming the Fe K reverberation for a black hole mass of $2 \times 10^7 M_{\odot}$ (with a factor of 2 uncertainty) (T. J. Turner et al. 2002).

4. MODELLING

4.1. Time-averaged spectrum

We performed a spectral analysis to account for the reflection dependency of the source. Previous analysis showed that the X-ray spectrum contains a relatively narrow Fe K line (M. L. Parker et al. 2018; G. A. Matzeu et al. 2020) as shown in Figure 2, reproduced here from the ratio of the spectrum to a simple powerlaw model. We carried out iron-line spectroscopy to constrain some

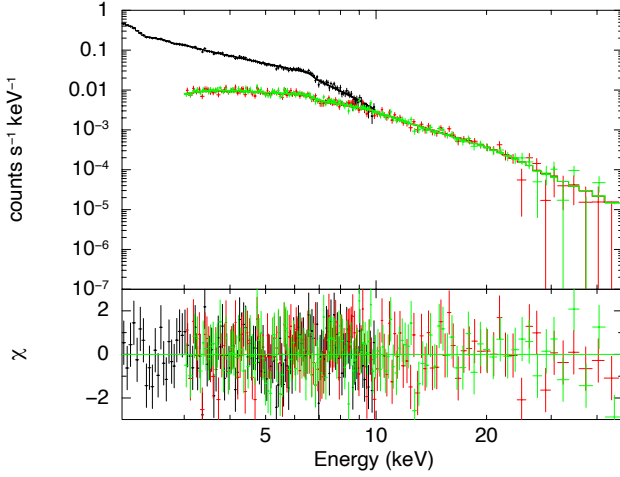


Figure 6. Time-averaged spectra of Ton S180 produced from *XMM-Newton* and *NuSTAR* observations. The spectra are fitted simultaneously using the relativistic reflection model `relxill1lp` (see text).

key physical parameters, with particular focus on the black hole spin.

We therefore fitted the time-averaged spectrum in XSPEC using the `relxill1lp` component of the relativistic reflection model `relxill` (J. García et al. 2014; T. Dauser et al. 2014), which convolves the X-ray spectrum being due to reflection from the disc as a result of irradiation from the X-ray source, described by `xillver` (J. García et al. 2013), with the relativistic ray-tracing code `relline` (T. Dauser et al. 2013) which accounts for the gravitational redshifts and Doppler shifts that cause relativistic broadening. We used the `Tbabs` model (J. Wilms et al. 2000) to take into account the galactic absorption. The fit was performed over a broadband spectral coverage inclusive of *XMM-Newton* observation simultaneously with that from *NuSTAR*. Combining the *NuSTAR* observation with *XMM-Newton* the spectral resolution can be maximized together with the photon count across 3–50 keV. We used a cross-calibration constant between the two instruments, fixing at 1 for *XMM-Newton* while left free for *NuSTAR*. The soft X-rays in Ton S180 are contributed by multiple components, including thermal emission from the accretion disc, Comptonized emission from the warm and optically thick corona. While describing the broadband spectrum by the reflection model, there occurs a mismatch between the fits of the thermal emission and reflection, as both are responsible for different physical processes, causing an inappropriate measurement of the black hole spin (M. L. Parker et al. 2018; G. A. Matzeu et al. 2020). Therefore, to place a cleanest measurement on the reflection spectrum and hence the spin, we fitted the spec-

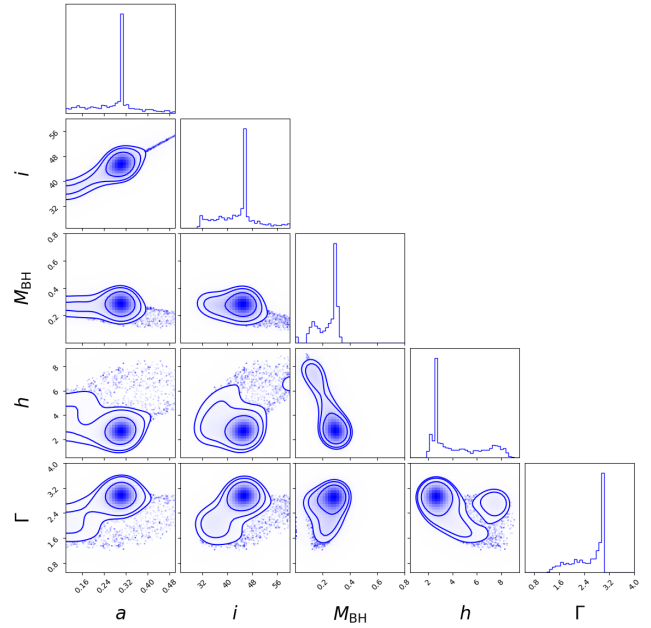


Figure 7. Corner plots of the MCMC parameters obtained from the relativistic transfer function modeling. The one-dimensional histograms represent the posterior probability distribution, which are normalized to have total area of one. Shown are the black hole spin a , inclination i (θ°), black hole mass M_{BH} ($\times 10^8 M_\odot$), coronal height h (r_g) and photon index Γ .

trum over the 2–50 keV band (see also A. Zoghbi et al. 2012; D. R. Wilkins et al. 2021, for example).

The relativistic reflection model `relxill1lp` provided a good fit to the broadband spectrum, providing a reduced $\chi^2/\text{d.o.f.} = 366/380$. Our simultaneous fit to the *XMM-Newton* and *NuSTAR* spectra provided constraints on the key physical parameters, the photon index Γ , iron abundance A_{fe} , coronal height h , and the ionization parameter $\log \xi$. We obtained the black hole spin at a low value $a = 0.43^{+0.10}_{-0.14}$ at an inclination of $42.72^{+1.51}_{-1.42}$ degrees. The reflection fraction has been found to be $R = 1.54^{+0.27}_{-0.36}$, which is moderately high, implying a strong reflection dependency of the source. During the fit, we fixed the inner radius at $1r_g$, the outer radius at $400r_g$, and the emissivity indices at the classical value of $q = 3$ (see G. A. Matzeu et al. 2020). The best-fit parameters are shown in Table 1. We show the modelled spectra from *XMM-Newton* and *NuSTAR* in Figure 6.

4.2. lag-energy spectrum

The intrinsic powerlaw continuum arising from the corona and the reflection-dominated emission from the accretion disc are generally expected to be observed with a certain time delay, as seen in the lag frequency or lag energy spectra. However, in reality, the flux of both

Table 1. Parameters obtained from the fits of *XMM-Newton* and *NuSTAR* spectra. All parameters are tied between the two detections. During analysis the multiplying constant is fixed at 1 for *XMM-Newton* and left free for *NuSTAR*. Galactic absorption is fixed at $N_H = 1.3 \times 10^{22} \text{ cm}^{-2}$. The 2–10 keV luminosity is obtained to be $3.16 \times 10^{43} \text{ erg s}^{-1}$.

N_H	Γ	a (GM/c^2)	i (degree)	$\log \xi$ $\text{log}(\text{erg cm s}^{-1})$	A_{fe} Fe/solar	R	h r_g	$\chi^2/\text{d.o.f}$
$1.3 \times 10^{22} \text{ cm}^{-2}$ (f)	$2.32_{-0.02}^{+0.02}$	$0.43_{-0.14}^{+0.10}$	$42.72_{-1.42}^{+1.51}$	$2.65_{-0.28}^{+0.10}$	$1.29_{-0.26}^{+0.38}$	$1.54_{-0.36}^{+0.27}$	$2.57_{-0.31}^{+0.44}$	366/380

emissions contributes to each band, diluting the absolute value of the measured lag, known as the lag dilution effect (see also P. Uttley et al. 2014). It is difficult to separate out the components of the direct continuum and the reflected emission because of the lack of high-cadence observations with the current detectors. This is generally the case for optical reverberation mapping, where lightcurves from low and high-cadence observations can be used to separate out lags due to two physical processes. Even in Fourier space, X-ray/UV/Optical reverberation mapping has recently used reverberation modeling to decouple the reprocessing lag and the BLR continuum lag (e.g. E. M. Cackett et al. 2022).

X-ray reverberation modeling is yet another powerful approach that has been performed in Fourier space. We used the relativistic transfer function model `kynreverb`⁶ (M. D. Caballero-García et al. 2018) to the observed lag-energy spectra, in which Fe K lag peaks (see Figure 3). The model relies on the full treatment of the general relativistic effect around an accreting black hole, allowing one to measure the path length difference between the disc and the corona to the rest frame observer. Disc reflections from each radius of the ionised disc are estimated from the reflection table `xillver` (J. García et al. 2013; T. Dauser et al. 2014) or `reflionx` (R. R. Ross & A. C. Fabian 2005). We fitted the two lag energy spectra simultaneously in `XSPEC`. In the fit, a few parameters were fixed to the values obtained from our fits of the time-averaged spectrum, including the iron abundance (A_{fe}) and 2–10 keV luminosity at $3.16 \times 10^{43} \text{ erg s}^{-1}$. Additionally, we fixed the inner radius (R_{in}) at $1r_g$, and the outer radius (R_{out}) at $400r_g$ similar to the time-averaged spectrum (see Section 4.1). The photon index (Γ), black hole spin (a), coronal height (h), mass of the black hole (M_{BH}), disc inclination (i) are left free to vary independently, which have been constrained at $\Gamma > 1.88$, $a = 0.30_{-0.17}^{+0.34} GM/c^2$, $h = 2.59_{-0.33}^{+5.17} r_g$, $M_{BH} = 0.29_{-0.16}^{+0.01} \times 10^8 M_\odot$ and $i = 45.40_{-7.82}^{+16.81} \text{ }^\circ$. The fit provided the electron density of the disc at $n_d = 16.04_{-0.52}^{+1.20} \times 10^{15} \text{ cm}^{-3}$, consistent with the previous measurements 15.6 cm^{-3} (J. Jiang et al.

Table 2. Best fit parameters from the transfer function modeling. The errors have been estimated at 68.27% confidence interval. The parameters are photon index Γ , inclination i , coronal height h , black hole mass M_{BH} , and spin a .

Γ	i (degree)	h (r_g)	M_{BH} ($10^7 M_\odot$)	a (GM/c^2)
> 1.88	$45.40_{-7.82}^{+16.81}$	$2.59_{-0.33}^{+5.17}$	$0.29_{-0.16}^{+0.01}$	$0.30_{-0.17}^{+0.34}$

2019) and $< 16 \text{ cm}^{-3}$ (G. A. Matzeu et al. 2020). The parameters provided by the lag spectra are found to be within the uncertainties of those obtained from the flux spectrum, in particular, both fits provided a relatively lower value of the black hole spin. The timing-based parameters are listed in Table 2. The best-fit modelling provided a reduced $\chi^2/\text{d.o.f.} = 16/12$. We present the best-fit modelled spectra in Figure 3.

The errors on the parameters obtained from the time-averaged spectrum and the lag spectra were estimated at 68.27% confidence by performing a Markov Chain Monte Carlo (MCMC) analysis. We used the Jeremy Sanders `XSPEC_EMCEE`⁷ code in `XSPEC`, which is a pure Python implementation of the Goodman & Weare’s Affine Invariant MCMC Ensemble sampler. For analysis, we used 50 walkers with 10,000 iterations and burned the first 1000 from the MCMC chain. We produce the corners of the MCMC parameters obtained from the transfer function modeling and plot their posterior distributions in Figure 7.

5. DISCUSSION

We have detected the reverberation of the Fe K emission line for the first time in the Narrow-line Seyfert 1 galaxy Ton S180. Generally, the Fe K emission feature appears as a clean part of the X-ray band where absorptions and other effects are less, providing an opportunity to place a robust measurement of the reverberation delay. We find that Fe K lag peaks at $\sim 117 \text{ s}$, calculated for the frequency range $(0.3 - 8.5) \times 10^{-4} \text{ Hz}$. The lag drops significantly as the frequencies are increased, allowing us to observe the lag amplitude of $\sim 22 \text{ s}$ at the

⁶ <https://projects.asu.cas.cz/stronggravity/kynreverb>

⁷ https://github.com/jeremysanders/xspec_emcee

highest Fourier frequencies of $(8.5 - 30) \times 10^{-4}$ Hz – suggesting that the underlying emission arises closer to the black hole.

Fe K emission line in Ton S180 has been confirmed in its X-ray spectrum. Using Fe K line spectroscopy, the black hole spin was constrained to ~ 0.98 , obtained by D. J. Walton et al. (2013). Later observation with *XMM-Newton* (~ 141 ks duration) showed that the emission feature is relatively narrow, which in turn favours the low spin value (< 0.4) constrained from the spectral modelling (M. L. Parker et al. 2018). The 0.3–10 keV X-ray spectrum cannot be accounted for entirely reflection dominated where the soft X-ray band requires fitting for Comptonisation of the seed photons and the thermal emission. The recent analysis of broadband spectra covering the *XMM-Newton* and *NuSTAR* bands has shown similar spectral properties, providing a low spin value (< 0.34) (G. A. Matzeu et al. 2020). However, reverberation modelling using a relativistic transfer function is another effective approach, which provides a timing-based result, allowing for an independent measure on the key physical parameters, spin and mass of the black hole (see e.g. W. N. Alston et al. 2020). However, this is generally applicable in sources showing reverberating X-ray features. Our reverberation modelling has put constraints on the black hole spin at $a = 0.30_{-0.17}^{+0.34}$ – consistent with the value from the spectral fit, $a = 0.43_{-0.14}^{+0.10}$. We have been able to constrain the black hole mass at $0.29_{-0.16}^{+0.01} \times 10^8 M_\odot$, the uncertainties of which are comparable to the previous measurement by T. J. Turner et al. (2002). Furthermore, it has been found that the other parameters from the lag spectra are within error bars of those obtained from the spectral fit.

We notice that there appears degeneracy between the black hole mass M_{BH} and the height h of the corona measured from the reverberation modelling for Ton S180. Inherent degeneracy between the height and black hole mass is not unusual, as it has been seen in previous reverberation modelling results, showing a static picture (e.g. D. Emmanoulopoulos et al. 2011; P. Chainakun et al. 2016; A. Ingram et al. 2019). However, this could possibly be overcome by performing joint modelling of multiple spectra obtained from numerous observations. Simultaneous modelling of the lag spectra from 16 long *XMM-Newton* observations (~ 130 ks per orbit) breaks this inherent degeneracy, providing a significant constraint on the black hole mass and coronal height (see W. N. Alston et al. 2020). Spectral fitting results also pointed out that degeneracy also persists be-

tween black hole spin a and disc inclination i (see M. L. Parker et al. 2018, Figure 3), where above the 3σ confidence level the upper limit of the spin is insignificant and rules out the maximal rotation of the black hole. The degeneracy appears even at 1σ confidence. Even using reverberation modelling, we have not been able to break the degeneracy. In future multi-epoch observations will likely to help break the degeneracies.

Ton S180 has been observed in four different epochs by *XMM-Newton* of which only the longer observation with ~ 141 ks exposure obtained in 2015 allowed us to detect the reverberation feature for the first time in this source. In future, a complete picture on the coronal geometry and dynamics of the inner accretion flow can be explored using multi-epoch observations with quite long exposures. Understanding coronal geometry also becomes feasible with the *IXPE* (M. C. Weisskopf et al. 2022), but it has some limitations, so far observing only a few bright Seyfert galaxies. The upcoming *eXTP* (P. Zhou et al. 2025) with four times effective area and better sensitivity than *IXPE* and *NewAthena* (M. Cruise et al. 2025) are expected to allow robust spectral-timing and polarimetric analysis to provide detailed information on the geometry of the accretion flow and the nature of the corona.

ACKNOWLEDGMENTS

We thank the anonymous referee for the constructive comments that have improved the manuscript. This research has made use of data and software provided by the High Energy Astrophysics Science Archive Research Center (HEASARC), which is a service of the Astrophysics Science Division at NASA/GSFC. DKR acknowledges IUCAA, Pune for the support in this work. SB acknowledges support from China Postdoctoral Science Foundation General Fund (grant no. 404985), Shanghai Postdoctoral Excellence Program (grant no. 2024686), and National Foreign Expert Project, Ministry of Science and Technology (grant no. 20240238). RS acknowledges the associateship program of IUCAA, Pune. VJ acknowledges the support provided by the Department of Science and Technology (DST) under the ‘Fund for Improvement of S & T Infrastructure (FIST)’ program (SR/FST/PS-I/2022/208). VJ also thanks the Inter-University Centre for Astronomy and Astrophysics (IUCAA), Pune, India, for the Visiting Associateship.

Facilities: *XMM-Newton*

Software: Astropy (Astropy Collaboration et al. 2013, 2018), numpy, scipy, matplotlib

REFERENCES

Alston, W. N., Parker, M. L., Markevičiūtė, J., et al. 2015, MNRAS, 449, 467, doi: [10.1093/mnras/stv351](https://doi.org/10.1093/mnras/stv351)

Alston, W. N., Fabian, A. C., Kara, E., et al. 2020, Nature Astronomy, 4, 597, doi: [10.1038/s41550-019-1002-x](https://doi.org/10.1038/s41550-019-1002-x)

Arévalo, P., McHardy, I. M., & Summons, D. P. 2008, MNRAS, 388, 211, doi: [10.1111/j.1365-2966.2008.13367.x](https://doi.org/10.1111/j.1365-2966.2008.13367.x)

Arévalo, P., & Uttley, P. 2006, MNRAS, 367, 801, doi: [10.1111/j.1365-2966.2006.09989.x](https://doi.org/10.1111/j.1365-2966.2006.09989.x)

Astropy Collaboration, Robitaille, T. P., Tollerud, E. J., et al. 2013, A&A, 558, A33, doi: [10.1051/0004-6361/201322068](https://doi.org/10.1051/0004-6361/201322068)

Astropy Collaboration, Price-Whelan, A. M., Sipőcz, B. M., et al. 2018, AJ, 156, 123, doi: [10.3847/1538-3881/aabc4f](https://doi.org/10.3847/1538-3881/aabc4f)

Caballero-García, M. D., Papadakis, I. E., Dovčiak, M., et al. 2018, MNRAS, 480, 2650, doi: [10.1093/mnras/sty1990](https://doi.org/10.1093/mnras/sty1990)

Cackett, E. M., Bentz, M. C., & Kara, E. 2021, iScience, 24, 102557, doi: [10.1016/j.isci.2021.102557](https://doi.org/10.1016/j.isci.2021.102557)

Cackett, E. M., Fabian, A. C., Zoghbi, A., et al. 2013, ApJL, 764, L9, doi: [10.1088/2041-8205/764/1/L9](https://doi.org/10.1088/2041-8205/764/1/L9)

Cackett, E. M., Zoghbi, A., & Ulrich, O. 2022, ApJ, 925, 29, doi: [10.3847/1538-4357/ac3913](https://doi.org/10.3847/1538-4357/ac3913)

Chainakun, P., Young, A. J., & Kara, E. 2016, MNRAS, 460, 3076, doi: [10.1093/mnras/stw1105](https://doi.org/10.1093/mnras/stw1105)

Cruise, M., Guainazzi, M., Aird, J., et al. 2025, Nature Astronomy, 9, 36, doi: [10.1038/s41550-024-02416-3](https://doi.org/10.1038/s41550-024-02416-3)

Crummy, J., Fabian, A. C., Gallo, L., & Ross, R. R. 2006, MNRAS, 365, 1067, doi: [10.1111/j.1365-2966.2005.09844.x](https://doi.org/10.1111/j.1365-2966.2005.09844.x)

Dauser, T., Garcia, J., Parker, M. L., Fabian, A. C., & Wilms, J. 2014, MNRAS, 444, L100, doi: [10.1093/mnrasl/slu125](https://doi.org/10.1093/mnrasl/slu125)

Dauser, T., Garcia, J., Wilms, J., et al. 2013, MNRAS, 430, 1694, doi: [10.1093/mnras/sts710](https://doi.org/10.1093/mnras/sts710)

De Marco, B., Ponti, G., Cappi, M., et al. 2013, MNRAS, 431, 2441, doi: [10.1093/mnras/stt339](https://doi.org/10.1093/mnras/stt339)

de Marco, B., Ponti, G., Uttley, P., et al. 2011, MNRAS, 417, L98, doi: [10.1111/j.1745-3933.2011.01129.x](https://doi.org/10.1111/j.1745-3933.2011.01129.x)

Emmanoulopoulos, D., McHardy, I. M., & Papadakis, I. E. 2011, MNRAS, 416, L94, doi: [10.1111/j.1745-3933.2011.01106.x](https://doi.org/10.1111/j.1745-3933.2011.01106.x)

Fabian, A. C., Zoghbi, A., Ross, R. R., et al. 2009, Nature, 459, 540, doi: [10.1038/nature08007](https://doi.org/10.1038/nature08007)

García, J., Dauser, T., Reynolds, C. S., et al. 2013, ApJ, 768, 146, doi: [10.1088/0004-637X/768/2/146](https://doi.org/10.1088/0004-637X/768/2/146)

García, J., Dauser, T., Lohfink, A., et al. 2014, ApJ, 782, 76, doi: [10.1088/0004-637X/782/2/76](https://doi.org/10.1088/0004-637X/782/2/76)

George, I. M., & Fabian, A. C. 1991, MNRAS, 249, 352, doi: [10.1093/mnras/249.2.352](https://doi.org/10.1093/mnras/249.2.352)

Haardt, F., & Maraschi, L. 1991, ApJL, 380, L51, doi: [10.1086/186171](https://doi.org/10.1086/186171)

Ingram, A., Mastroserio, G., Dauser, T., et al. 2019, MNRAS, 488, 324, doi: [10.1093/mnras/stz1720](https://doi.org/10.1093/mnras/stz1720)

Jiang, J., Fabian, A. C., Dauser, T., et al. 2019, MNRAS, 489, 3436, doi: [10.1093/mnras/stz2326](https://doi.org/10.1093/mnras/stz2326)

Kara, E., Alston, W. N., Fabian, A. C., et al. 2016a, MNRAS, 462, 511, doi: [10.1093/mnras/stw1695](https://doi.org/10.1093/mnras/stw1695)

Kara, E., Fabian, A. C., Cackett, E. M., Miniutti, G., & Uttley, P. 2013a, MNRAS, 430, 1408, doi: [10.1093/mnras/stt024](https://doi.org/10.1093/mnras/stt024)

Kara, E., Fabian, A. C., Cackett, E. M., et al. 2013b, MNRAS, 434, 1129, doi: [10.1093/mnras/stt1055](https://doi.org/10.1093/mnras/stt1055)

Kara, E., Miller, J. M., Reynolds, C. S., & Dai, L. J. 2016b, in AAS/High Energy Astrophysics Division, Vol. 15, AAS/High Energy Astrophysics Division #15, 100.06

Kara, E., Steiner, J. F., Fabian, A. C., et al. 2019, Nature, 565, 198, doi: [10.1038/s41586-018-0803-x](https://doi.org/10.1038/s41586-018-0803-x)

Lohfink, A. M., Reynolds, C. S., Mushotzky, R. F., & Nowak, M. A. 2013, Mem. Soc. Astron. Italiana, 84, 699, doi: [10.48550/arXiv.1301.4997](https://doi.org/10.48550/arXiv.1301.4997)

Marinucci, A., Matt, G., Kara, E., et al. 2014, MNRAS, 440, 2347, doi: [10.1093/mnras/stu404](https://doi.org/10.1093/mnras/stu404)

Matzeu, G. A., Nardini, E., Parker, M. L., et al. 2020, MNRAS, 497, 2352, doi: [10.1093/mnras/staa2076](https://doi.org/10.1093/mnras/staa2076)

McHardy, I. M., Arévalo, P., Uttley, P., et al. 2007, MNRAS, 382, 985, doi: [10.1111/j.1365-2966.2007.12411.x](https://doi.org/10.1111/j.1365-2966.2007.12411.x)

Miller, L., Turner, T. J., Reeves, J. N., & Braito, V. 2010a, MNRAS, 408, 1928, doi: [10.1111/j.1365-2966.2010.17261.x](https://doi.org/10.1111/j.1365-2966.2010.17261.x)

Miller, L., Turner, T. J., Reeves, J. N., et al. 2010b, MNRAS, 403, 196, doi: [10.1111/j.1365-2966.2009.16149.x](https://doi.org/10.1111/j.1365-2966.2009.16149.x)

Miyamoto, S., & Kitamoto, S. 1989, Nature, 342, 773, doi: [10.1038/342773a0](https://doi.org/10.1038/342773a0)

Nowak, M. A., Vaughan, B. A., Wilms, J., Dove, J. B., & Begelman, M. C. 1999, ApJ, 510, 874, doi: [10.1086/306610](https://doi.org/10.1086/306610)

Parker, M. L., Miller, J. M., & Fabian, A. C. 2018, MNRAS, 474, 1538, doi: [10.1093/mnras/stx2861](https://doi.org/10.1093/mnras/stx2861)

Reynolds, C. S., & Nowak, M. A. 2003, PhR, 377, 389, doi: [10.1016/S0370-1573\(02\)00584-7](https://doi.org/10.1016/S0370-1573(02)00584-7)

Ross, R. R., & Fabian, A. C. 2005, MNRAS, 358, 211, doi: [10.1111/j.1365-2966.2005.08797.x](https://doi.org/10.1111/j.1365-2966.2005.08797.x)

Shakura, N. I., & Sunyaev, R. A. 1973, A&A, 24, 337

Tripathi, S., Misra, R., Dewangan, G., & Rastogi, S. 2011, ApJL, 736, L37, doi: [10.1088/2041-8205/736/2/L37](https://doi.org/10.1088/2041-8205/736/2/L37)

Turner, T. J., Romano, P., Kraemer, S. B., et al. 2002, ApJ, 568, 120, doi: [10.1086/338925](https://doi.org/10.1086/338925)

Uttley, P., Cackett, E. M., Fabian, A. C., Kara, E., & Wilkins, D. R. 2014, *A&A Rv*, 22, 72, doi: [10.1007/s00159-014-0072-0](https://doi.org/10.1007/s00159-014-0072-0)

Walton, D. J., Nardini, E., Fabian, A. C., Gallo, L. C., & Reis, R. C. 2013, *MNRAS*, 428, 2901, doi: [10.1093/mnras/sts227](https://doi.org/10.1093/mnras/sts227)

Wang, J., Kara, E., Lucchini, M., et al. 2022, *ApJ*, 930, 18, doi: [10.3847/1538-4357/ac6262](https://doi.org/10.3847/1538-4357/ac6262)

Weisskopf, M. C., Soffitta, P., Baldini, L., et al. 2022, *Journal of Astronomical Telescopes, Instruments, and Systems*, 8, 026002, doi: [10.1111/1.JATIS.8.2.026002](https://doi.org/10.1111/1.JATIS.8.2.026002)

Wilkins, D. R., Gallo, L. C., Costantini, E., Brandt, W. N., & Blandford, R. D. 2021, *Nature*, 595, 657, doi: [10.1038/s41586-021-03667-0](https://doi.org/10.1038/s41586-021-03667-0)

Wilkins, D. R., Gallo, L. C., Silva, C. V., et al. 2017, *MNRAS*, 471, 4436, doi: [10.1093/mnras/stx1814](https://doi.org/10.1093/mnras/stx1814)

Wilms, J., Allen, A., & McCray, R. 2000, *ApJ*, 542, 914, doi: [10.1086/317016](https://doi.org/10.1086/317016)

Zhou, P., Mao, J., Zhang, L., et al. 2025, arXiv e-prints, arXiv:2506.08367, doi: [10.48550/arXiv.2506.08367](https://doi.org/10.48550/arXiv.2506.08367)

Zoghbi, A., & Fabian, A. C. 2011, *MNRAS*, 418, 2642, doi: [10.1111/j.1365-2966.2011.19655.x](https://doi.org/10.1111/j.1365-2966.2011.19655.x)

Zoghbi, A., Fabian, A. C., Reynolds, C. S., & Cackett, E. M. 2012, *MNRAS*, 422, 129, doi: [10.1111/j.1365-2966.2012.20587.x](https://doi.org/10.1111/j.1365-2966.2012.20587.x)

Zoghbi, A., Reynolds, C., Cackett, E. M., et al. 2013, *ApJ*, 767, 121, doi: [10.1088/0004-637X/767/2/121](https://doi.org/10.1088/0004-637X/767/2/121)

Zoghbi, A., Uttley, P., & Fabian, A. C. 2011, *MNRAS*, 412, 59, doi: [10.1111/j.1365-2966.2010.17883.x](https://doi.org/10.1111/j.1365-2966.2010.17883.x)